On the operational use of UAVs for video-derived bathymetry

Erwin W.J. Bergsma, Rafael Almar, Luis Pedro Melo de Almeida, Moussa Sall

Version of Record: https://www.sciencedirect.com/science/article/pii/S0378383918303582
Manuscript_bca8604ab6f28b13ccfe037931b8c0f2

On the Operational Use of UAVs for Video-Derived Bathymetry

Erwin W.J. Bergsma[a], Rafael Almar[b], Luis Pedro Melo de Almeida[c], Moussa Sall[d]

[a] *CNES-LEGOS,UMR-5566, 14 Av. Edouard Belin, 31400, Toulouse, France ; erwin.bergsma@legos.obs-mip.fr*
[b] *IRD-LEGOS, UMR-5566, 14 Av. Edouard Belin, 31400, Toulouse, France ; rafael.almar@ird.fr*
[c] *Universidade Federal do Rio Grande, Rio Grande, Brasil; melolp@gmail.com*
[d] *Centre de Suivi Écologique, Dakar, Senegal; sall@cse.sn*

Abstract

Commercial Unmanned Areal Vehicles (UAV) are taking a flight: it has never been more accessible to own an UAV and as easy to operate one , e.g. a drone. For coastal monitoring these advances open a new world of monitoring such as inter-tidal beach topography through Structure for Motion. This paper aims to 1) show the potential of the UAV-based depth inversion with 2) limited georeferencing resources for rectification, comparing traditional field-based GCPs and fully remote standalone methods (few local GCPs and Google Earth derived GCPs) and a 3) novel automated error reduction inclusion for the breakpoint location. Unlike with shore-based cameras, image stabilisation is key airborne bathymetry estimation. At places that are hard to reach it is not always possible to get ground control points. We discuss the use of Google Earth to obtain ground control points. In all video-derived bathymetries obtained in this work, great overestimation of the depth is found around wave breaking which is often linked to a phase shift in pixel intensity (dark wave front to white foam). A new method to overcome phase shift issues around breaking is presented that results in a significant error reduction of 58% around the break point.

Keywords: UAV, Remote Sensing, bathymetry, nearshore

1. Introduction

Beaches morphology can be completely reshaped at the scale of a single storm but there is until now no easy technique to estimate bathymetry in the nearshore. At the same time, the need for an updated coastal bathymetry at socio-environmental hotspots (e.g. low lying exposed urban areas) is increasing with the development of integrated coastal management and risk assessment and engineering projects (e.g. dikes, harbours, nourishment, [1]). In particular, more and more research focuses on the assessment and short term prediction of storm impact which can induce large changes over short periods [2, 3, 4]. While shore-based video permanent cameras now provide reasonable continuous quantitative description of morphodynamics [5], their use is often limited to accessible areas (e.g. urban areas- high-rise building close to shore). Recently, UAVs have developed and offer a new potential of flexibility with easy, punctual measurements with limited logistics. In this sense, they are complementary to video-camera stations and/or conventional field measurements.

Recent technological advances, improved usability and declining material cost for UAVs creates a new era of nearshore remote sensing monitoring tools. Increasingly, topographies are obtained using Structure for Motion (SfM) with accuracies in the order of centimetres. Given the flexibility and easy usability (user friendly) of UAVs, the next step forward is to provide bathymetric information in addition to Structure for Motion topography, creating a continuum between land and sea. Efforts have been made to extend video-based bathymetry estimations fixed at shore, to airborne applications [6].

Commonly, wave physics-based video-derived bathymetries are estimated using either wave dissipation patterns in combination with numerical models or wave propagation. The latter is used here and utilises the mathematical dispersion relation between wave celerity and depth, either in a linear or non-linear form. For the linear dispersion relation it requires two of the five variables (c, T, L, k, ω) to solve the problem set, for the non-linear dispersion relation wave amplitude (or height) should be known. One can choose to stay in the time domain [7] or convert to spectral domain [8, 9, 10]. Shore-based systems are typically capable of estimating bathymetry O(10's cm) accurately [10, 11].

In this paper, we provide a bathymetry derived from an UAVs using a spectral method described in Holman et al. [10]. The estimate is compared

with echosounder survey conducted in Saint Louis beach, Senegal (West Africa) in 2016 within the framework of the COASTVAR experiment. A method to rectify images without the need of locally measured ground control points is introduced. The correction for drone movements is discussed as well as a simple image pre-processing method that can improve classical optical modulation transfer function (MTF) issues linked to the breakpoint signal common to optical video methods in the nearshore.

2. Methodology

2.1. Study site and data collection

The city of Saint Louis is located in Northern part of Senegal, in the West of Africa. It is situated on the 10-km long, Langue de Barbarie, sandspit at the mouth of the Senegal river. The city is classified as a world heritage historic city and the surrounding area is part of the National Parc of Langue de Barbarie, the largest Marine Protected Area in Senegal. The city population (mostly composed by fishermen) is increasing at a fast rate, and currently faces an intensification of environmental problems due to coastal erosion. This stretch of coast is described as drift-aligned shoreline by [12], which is mainly driven by one of the strongest alongshore sediment transport rates in the world, comprised between 0.5 and $1Mm^3$ per year.

This coastal area faces energetic waves, generally from an oblique incidence angle (annual average wave conditions are $H_s = 1.52$ m, $T_p = 9.23$ s, Dir = 325 degrees [13]), with more energetic conditions in winter with long swells coming from distant North Atlantic. Sediment grain size is intermediate (0.2 mm) and the beach is most of the time barred with a low tide terrace and a steep upper part. Tide is diurnal and micro-tidal (between 0.4 and 1.6 for neap to spring conditions, respectively).

In December of 2016, a field experiment was performed in Saint Louis beach, with the aim to quantify the processes responsible for the observed erosion. This experiment builds on ongoing efforts to quantify the long-term shoreline evolution of this coastal area based on satellite imagery [13, 12, 14]. The field experiment lasted from the 4th to 13th of December 2016, and involved about 30 participants from several countries, and included numerous instruments, among which several Acoustic Doppler Current Profilers, Pressure Transducers, echo-sounding bathymetries, RTK-GPS topographies, Structure for Motion topographies, high-detailed LiDAR measurements and video capturing of the swash zone. The bathymetry serves as a ground-truth

and is measured with a single-beam echosounder by the French Navy (SHOM - Naval Hydrographic and Oceanographic Service) outside the surfzone (accuracy 10-15 cm). Within in the surfzone (subject to heaving breaking) a single beam echosounder was used attached to a surfboard to obtain depth information. Due to the heavy wave-breaking the accuracy reduces to 10s of centimetres, which is similar to jet-ski surveys in these environments. In the shallowest part of the nearshore zone, an on-foot D-GPS survey links the bathymetry to the topography (accuracy 3-5 cm).

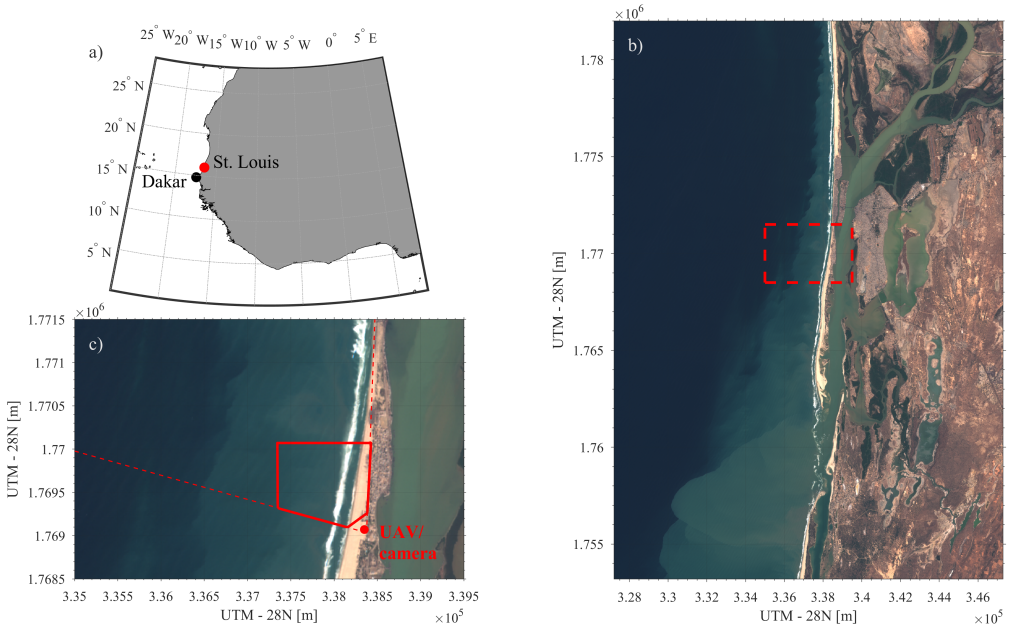

Figure 1: Geo-location of the field experiment at St. Louis. a) An overview of West-Africa (WGS84) in which the capital of Senegal (Dakar) is highlighted with the black dot likewise the red dot indicates the study site (St. Louis), b) Shows an ESA-Sentinel II image (UTM) covering the regional situation around St. Louis taken on 9 December 2016 11:34 AM local time. The red-dashed lines indicate the zoomed area shown in c). c) shows the local area around the study site in which the red-dashed line indicates the field of view of the camera, the red-dot indicates the position of the UAV and the red-box represents the depth estimation domain.

Drone imagery was also collected every day to estimate beach topography with stereoscopy method and bathymetry, measuring waves characteristics from stationary flights. Images are collected using a DJI Phanthom 3-pro UAV equipped with the standard off-the-shelf camera. As a rule of thumb for

shore-based video systems, the camera should be placed as high as possible for better results. Bearing this in mind and considering a safe altitude to fly the drone, we aimed to fly the drone at 125 m altitude. In-flight, 11 to 12 minute videos (depending on the battery life) were recorded at 50 Hz frequency with a resolution of 1920 x 1080 pixels. As part of the post-processing videos are down-sampled to approximately 3 Hz.

2.2. UAV related image-processing

After take-off, the UAV is manoeuvred to a certain position and is supposed to hover at a stationary position with fixed view angles during the video-recording time. In order to assess if the position and orientation of the UAV are truly fixed we derived mean pixel intensity image over the duration of the video-file (Timex). A sharp image indicates limit movement and (re)orientation and vice versa for a blurred image result. The Timex-image presented in Figure 2a shows a blurred image suggesting inadmissible variability, either low-frequency UAV movements such as repositioning or high-frequency vibrations. It is interesting to note that these image-related variabilities have an amplified effect, O(10s metres), on the real-world positioning of the pixels when the image is rectified on a horizontal plane in the real-world. These movements on the horizontal plane lead to even greater, unacceptable, positioning errors. Hence, in this case image stabilisation is required.

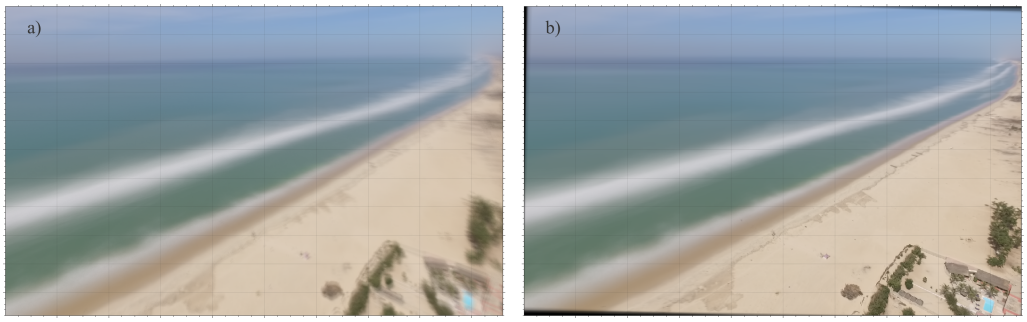

Figure 2: Timex images captured from the UAV-flight. a) Shows the Timex derived from the raw video data. b) represents a Timex images obtained after stabilisation of the video-frames.

The drone image-stabilising have been performed by applying MatLAB image-processing tools, following this sequence of procedures: 1. identify and

match distinct features in two consecutive video-frames using the maximum correlation between a subset of pixels around a GCP and the new image, 2. compute a scaled affine translation-rotation matrix and 3. translate/rotate the second image to match the first image. In addition, we added horizon tracking because most of the distinct features are located the bottom-right extremes of the video-frames which introduces a bias. In this case, MatLAB's imaging-toolbox feature detection routines do not recognise the horizon as a distinct feature. To overcome this issue the horizon is identified using the methodology presented by Schwendeman and Thomson [15]. For each video-frame the horizon is automatically found by deploying an edge-filter in combination with a Hough-transform. The found horizon is then fed into stage two of the stabilisation process. Figure 2b shows the improved Timex image after stabilisation. Compared to Figure 2a, Figure 2b clearly shows the estate in the bottom right corner of the image, as well as settlements Northwards along the coast. It is interesting to note that after applying the image-stabilisation is possible to identify a double bar system in the North part of the coast, while previous instabilities disguised it's existence.

2.3. Photogrammetric approach

Video-frame pixels (U, V) can be linked to a real-world coordinate (x, y, z) through a projective transformation, in this case projected on a tide-fixed horizontal plane. Here, we use a linear homogeneous projective transformation ($x' = Px$) between pixels and real-world projection as described in Hartley and Zisserman [16] and outlined by Holman et al. [6]. Here x' are the 2D image coordinates U, V and x represents the 3D real-world coordinates (x, y, z). The homogeneous projective matrix P consists of three factor matrices K [6] :

$$P = KR\left[I| - C\right] \tag{1}$$

wherein K is known as the camera matrix and holds camera intrinsics, R represents a rotation matrix and $\left[I| - C\right]$ is a 3x3 identity matrix I augmented by C which contains the camera location in real-world coordinates (x, y, z). Matrix K, holding the camera intrinsics is obtained using the Caltech Camera Calibration Toolbox (`http://www.vision.caltech.edu/bouguetj/calib_doc/`):

$$K = \begin{bmatrix} f_U & S & U_0 \\ 0 & f_V & V_0 \\ 0 & 0 & 1 \end{bmatrix} \tag{2}$$

in which f represents the focal length in U and V, Skewness (S) and the centre of the image (U_0, V_0). The rotation matrix R contains orientation angles such as Azimuth (orientation to North), Tilt (nadir = 0) and Roll. In total (1) has 11 variables of which (2) solves 5 and thus this set of equations leaves 6 degrees of freedom. To solve this multi-degree of freedom problem set, a non-linear fitting is performed so that the 6-free values are found minimising it's squared error. To solve this 6DOF solution at least 3 GCPs are required as each GCP provides 2 knowns (U,V pixel coordinates).

2.4. Camera-movement / GCP tracking

Holman et al. [6] shows the UAV-movement (x, y, z) and camera-reorientation (azimuth, tilt, roll), a similar analysis is performed in this study. Camera movements and changing angles in time are obtained by (re-)calculating the 6-degrees of freedom for every frame using GPS-measured Ground Control Points (GCPs). Here, the GCPs targets (crosses) were laid out randomly spread over the field of view. The MatLAB imaging-processing toolbox routines could often not detect these GCPs as distinct features. Hence, to detect our GCP-targets, an alternative tracking is to be sought. Although the MatLAB routines do not find a distinct feature, the GCPs do represent a unique combination of pixel values which we presume to be transferable between video-frames. Meaning that if a pattern is identified in one video-frame it is likely to be found in a subsequent video-frame. To do so, a 2D-correlation analysis is applied, and the same patterns are recognised in different frames as shown in Figure 3.

Commonly, GCP locations are picked for a (first or representative) video-frame with the best possible accuracy on which the geometry is constructed, like the red-dots in Figure 3a. An area around the GCPs, in this case 30x20 pixels, is stored as a template for feature matching in subsequent video-frames (green square in Figure 3a). For each video-frame the templates are used to find the pixel position of the GCPs through a 2D correlation analysis (maximum correlation). The newly obtained GCP-positions in the video-frame are then used to recalculate the 6 degrees of freedom: x, y, z, azimuth, tilt and roll.

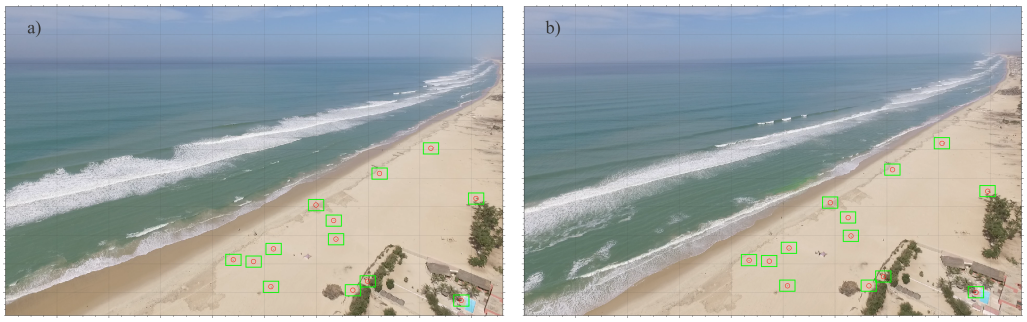

Figure 3: Example of Ground Control Point (GCP) tracking. a) shows the first frame of the video in which the red dots represent the GCPs as picked and the green squares are the template area. b) shows an arbitrary video-frame with automatically found GCPs positions (red dots).

2.5. Depth estimation

Since the 1940s efforts have been made to estimate bathymetry remotely using optical imagery, with the imagery obtained from land-based, airborne or spaceborne monitoring systems. Commonly, near-shore depths are estimated using the mathematical relation between wave celerity and depth which is valid in intermediate to shallow water depths, as presented in (3).

$$c^2 = \frac{\sigma^2}{k^2} = \frac{g}{k}\tanh\left(kh\right) + \vec{U}^2 \bullet k^2 \tag{3}$$

wherein c is wave celerity, σ is angular wave frequency, k represents the wave number, g is the gravitational acceleration, h is depth and $\vec{U}$ represents the mean current. To solve (3) for depth, one needs to measured two of free variables in spectral domain (c, k, ω) [8, 10, 11], or (c, L, T) in the temporal domain [7]. Here, we work in the spectral domain and apply depth inversion with non-gridded pixel positions (floating pixels) following [11] using the first two out of three phases of *cBathy*. To solve the linear dispersion relation *cBathy* seeks for wave frequency and wave number pairs. In phase I, frequencies are selected based on a local coherency criterion (N-most coherent frequencies are taken). For the selected frequencies a phase ramp is estimated to find wave-number (k). *cBathy*'s phase II then combines the selected frequencies so that an optimal fit with the linear dispersion relation is found, resulting in a single, combined depth estimate. It is important to note that not executing Phase III (Kalman Filtering), reduces robustness

[10, 11]. However, the strength of the Kalman filter depends on the multitude of available estimated bathymetries; generally the more data the stronger the Kalman results and in this study have few video-recordings.

3. Results

3.1. UAV movement and (re)orientation

Holman et al. [6] showed that over a set of 10 flights the mean standard deviation of their UAV movement in x, y, z was respectively 0.17 m, 0.24 m, and 0.53 m and similarly the mean standard deviation of the azimuth, tilt and roll angles was respectively 0.38°, 0.2° and 0.26°. With these values, Holman et al. [6] justifies the assumption of a fixed camera position. Here we assess the movements and (re)orientation of the camera following the GCP-tracking presented in Section 2.4. Figure 4 shows the results for the total number of 2048 video-frames.

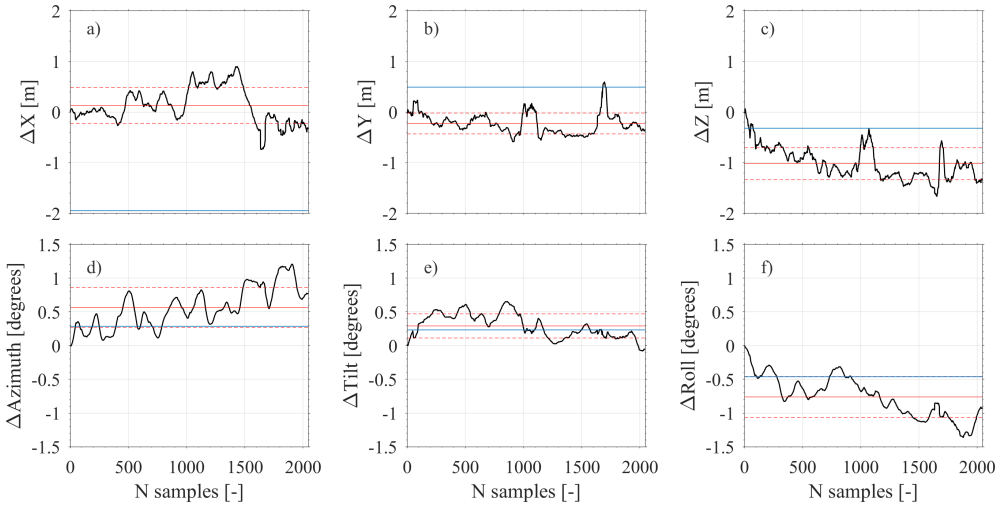

Figure 4: UAV movements (x, y, z) and (re)orientation (azimuth, tilt, roll) are respectively presetned in a-f for a full video of 2048 frames. The red lines indicate the mean and standard deviation per variable. The blue line represents values obtained by the UAV (constant for the total flight duration).

Figure 4a,b show that the UAV has quite a stable horizontal hovering position considering the maximum deviation of 0.9 m for ΔX and 0.55 m for ΔY. The maximum vertical offset ΔZ is slightly larger $\Delta Z_{max} = -1.5$ m and

Figure 4c shows drift over the video-duration downward. Reorientation of the UAV is for all angles within ±1.5 degrees. During the full video the UAV rotates horizontally in anti-clockwise direction while keeping the vertical view angle stable and rolling the image clockwise. In comparison to the average values found in Holman et al. [6], the found standard deviations in this work are larger; $\sigma_x = 0.32$ m, $\sigma_y = 0.24$ m, $\sigma_z = 0.22$ m, $\sigma_{azimuth} = 0.27°$, $\sigma_{tilt} = 0.17°$ and $\sigma_{roll} = 0.31°$. The found UAV movement and reorientation angles makes it unlikely to consider the UAV fixed over the duration of the full video. These movements and reorientations primarily lead to the blurred image as shown in Figure 2a and amplifies the need for stabilisation, however, the direct effect on depth estimation is scrutinised below. Besides the UAV-tracking, a single set of position and orientation values measured by the UAV can be obtained from the video. These values are presented by the blue solid line in Figure 4. Apart from the X position, measured and tracked values for the position are within 0.5 meters of the average and the UAV-stored angles are all within the tracking-related standard deviation.

Movements and view-angles should be near-fixed after the image-stabilisation. Camera movements and (re)-orientation are tracked after the stabilisation per sample (video-frame), shown in Figure 5. The effect of the image-stabilisation is particularly reducing the variability of the view-angles. The standard deviations over 2048 frames are reduced in comparison to the earlier found values for all angles: $\sigma_{azimuth} = 0.10°$, $\sigma_{tilt} = 0.07°$ and $\sigma_{roll} = 0.09°$. The image-stabilisation has a contrary effect on the x, y, z positioning: the standard deviations σ_x, σ_y, σ_z increased to respectively, 0.44 m, 0.30 m and

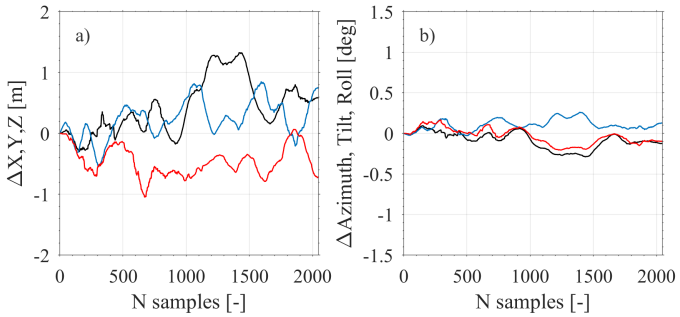

Figure 5: Tracked artificial movements of the UAV after image-stabilisation. a) represents the change in x (black), y (blue) and z (red) compared to the found x, y, z for the first frame while b) shows the resulting orientation angles (Azimuth (black), Tilt (blue) and Roll (red)) in comparison to the first frame.

0.24 m. It is important to note that in case of enough altitude (z), stable orientation-angles have greater priority than the x, y, z positioning (nonetheless important) to obtain a stable projective solution over 2048 frames. In other words, small changes in orientation-angles result in larger projective errors than small changes in x, y, z relative to the camera altitude. Considering the high altitude of the UAV (125 m) these standard deviations are considered acceptable.

3.2. Video-based bathymetry estimation from UAVs

Shore-based systems commonly do not perform image-stabilisation because they are considered fixed and they don't vibrate. If one assumes the drone to be fixed and without vibrations,one should be able to just apply depth inversion routines as suggested in Holman et al. [6]. One would expect that small instabilities would be cancelled out. However, Figure 6 shows otherwise in which c) indicates a significant over estimation in the nearshore and seaward the video-derived bathymetry is underestimated. RMS-errors are calculated over the whole domain (RMS_{all}), outside the surfzone (RMS_{os})

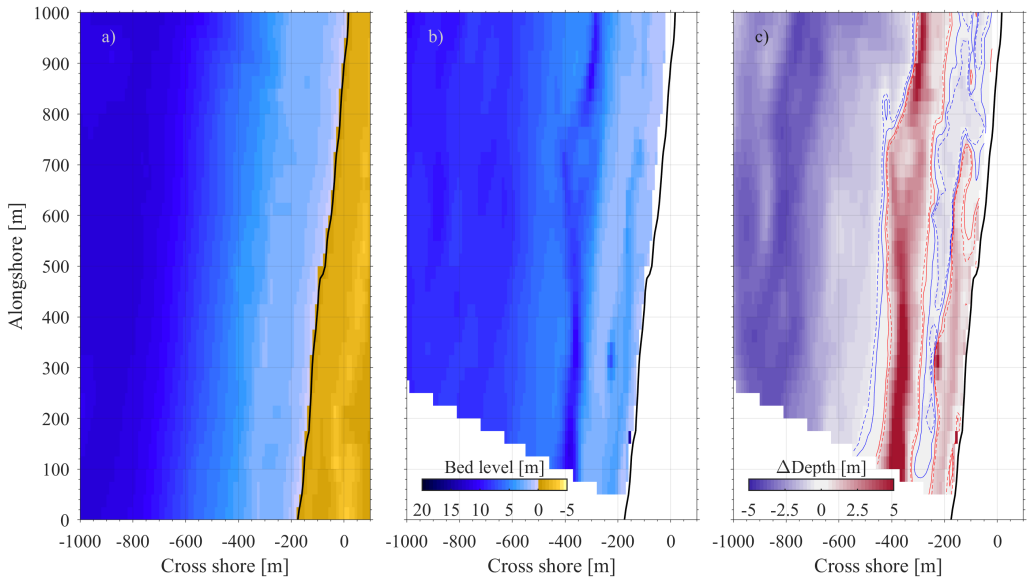

Figure 6: Depth inversion in comparison to the measured bathymetry. a) shows the measured bathymetry provided by SHOM. b) demonstrates the video-derived bathymetry from the unstabilised video and c) indicates the difference between the two in which positive values reflect overestimation of depth and vice versa.

and for $-800m < X < -500$ (RMS_{85}). For the unstabilised video we respectively find: $RMS_{all} = 2.35$ m, $RMS_{os} = 2.80$ m and $RMS_{85} = 2.55$ m. The RMS-errors show unacceptable differences of approximately 30% of the local waterdepth outside the surfzone. The red-band around $X = -400$ m correspond to the location of a sand-bar and hence inaccuracies due to wave transformation and breaking [7].

After image-stabilisation we have seen that the variance of the orientation angles were reduced significantly in Figure 5. A minimised variance of the orientation angles results in a significantly better estimated bathymetry, considering Figure 7a,b, particularly outside the surfzone reduced further away from the camera as mentioned in Section 3.1. Figure 7b shows less colouring and thus less difference in comparison to Figure 6c. Over the total domain the RMS-error remained constant $RMS_{all} = 2.35$ m but RMS_{os} reduced to 1.07 m and $RMS_{85} = 0.41$ m. Outside the surfzone this means that due to image-stabilisation 61% error-reduction is achieved. RMS_{85} shows a greater, 84% reduction in RMS-error.

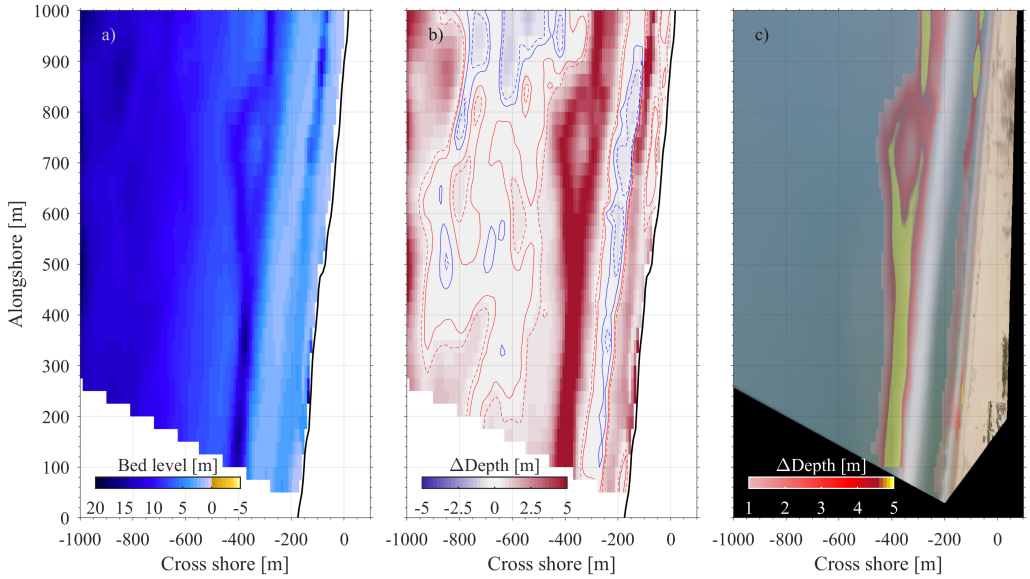

Figure 7: Depth inversion from the stabilised video a) show the video-derived bathymetry while b) compares a) to the measured bathymetry as shown in Figure 6a. c) represents the rectified image with the difference between estimated and measured depth on top.

Although we find an overall improvement and reduction of the RMS-error, around the break point an amplified difference between the measured

and estimated bathymetry is observed in Figure 7c. On the one hand this can be due to inaccurate in-situ measurements (least accurate around/in the surfzone) as the major contribution to the overall error occur just seaward breaking (the white-foam indicates breaking). On the other hand it could be related to the depth-derivation methodology.

4. Discussion

4.1. Bathymetry estimation without in-situ GCPs

Complete autonomous bathymetry estimation, without RTK-GPS measured GCPs, would be the ultimate solution in environments that are hard to reach. Internally measured values for the 6 degrees of freedom are currently not measured accurately enough to get a proper geometry (compared to the found UAV position with in-situ GCPs: $\Delta x = 4.05$ m , $\Delta y = -0.88$ m , $\Delta z = 4.5$ m, $\Delta azimuth = -4.5$ deg , $\Delta tilt = -3.62$ deg , $\Delta roll = 0.12$ deg). Tracking the horizon is shown in Figure 8 to be an effective tool to obtain the camera's roll. The roll is included as a known/constant variable in the R-matrix in equation 1). In addition, Google Earth is used to obtain addition GCP location information from identifiable points, such as buildings, fencing and hedges. The global elevation data that is used in Google Earth is composed of several datasets such as radar derived DEMs from NASA' Shuttle Radar Topography Mission (SRTM) and LiDAR. In Senegal, there is not such a hybrid approach and only SRTM is used. Depending on its version the global SRTM dataset is vertically accurate from 5.6 to 9 m [17]. In Africa the SRTM dataset has an accuracy of 5.6 m, which is not sufficiently accurate for GCPs. Considering that the beach at St. Louis is relatively flat and the accuracy of the SRTM dataset, the vertical elevation is set to zero and only the horizontal positioning is used for the 5 Google Earth based GCPs.

A bathymetry estimate using this approach is shown in Figure 9. Overall, the estimation using the horizon and Google Earth ground control points shows a similar order of accuracy in comparison to results obtained with in-situ measured GCPs. RMS_{all} is 1.91 m, RMS_{os} is 1.44 m, $RMS_{85} = 1.14$ m. The anomaly around the break point (white area in Figure 9c) is also visible in the bathymetry estimation in Figure 9a,b. Nontheless, the bathymetry estimation around the breaking-point is equally accurate compared to the results in Figure 7. Considering that the found error estimations are similar, we can suggest that in-situ GCPs are not an absolute necessity.

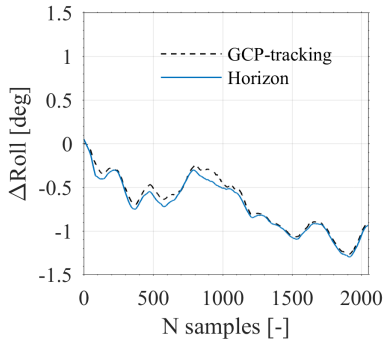

Figure 8: $\Delta Roll$ estimation using the GCP-tracking algorithm (dashed-black) and horizon identification (blue).

4.2. Break point anomaly

In all the results so far, a clear overestimation of the depth is found around the point of wave breaking. This effect is more often observed with shore-based systems and is thought be linked to the physical process of wave breaking and/or the observational limits of video cameras. The former relates to wave non-linearities as waves shoal before breaking and then break over the sandbar. The latter, relates to the Modulation Transfer Function (MTF). As waves shoal the camera registers a dark incident wave front, while when waves break, breaking-induced foam whitens the free surface. As one can imagine there is a sudden shift between minimal and maximal pixel intensities.

These differences in MTF-function are not an issue while computing wave phase as long it is spatio-temporally consistent. Hence, as pointed out above, problems arise at transition zones such as at the known issue at the break-point. Considering the sudden shift between pixel intensities a kind of normalisation between the phases would remove this anomaly. Considering a pure sinusoidal, phase-shifts by π (or multitude of π) can be removed by taking the absolute derivative. Here, we propose to take the absolute derivative of the time-varying pixel intensities in time. Taking the first derivative transforms the signal into a rate of pixel intensity change and the absolute makes it insensitive to the dark-to-bright or bright-to-dark transition, so a more consistent MTF function with or without breaking.

Considering the sudden shift between pixel intensities a quasi-normalisation between the phases would remove this anomaly. Here, we propose to take the absolute derivative of the time-varying pixel intensities in time. For stacks with this follows:

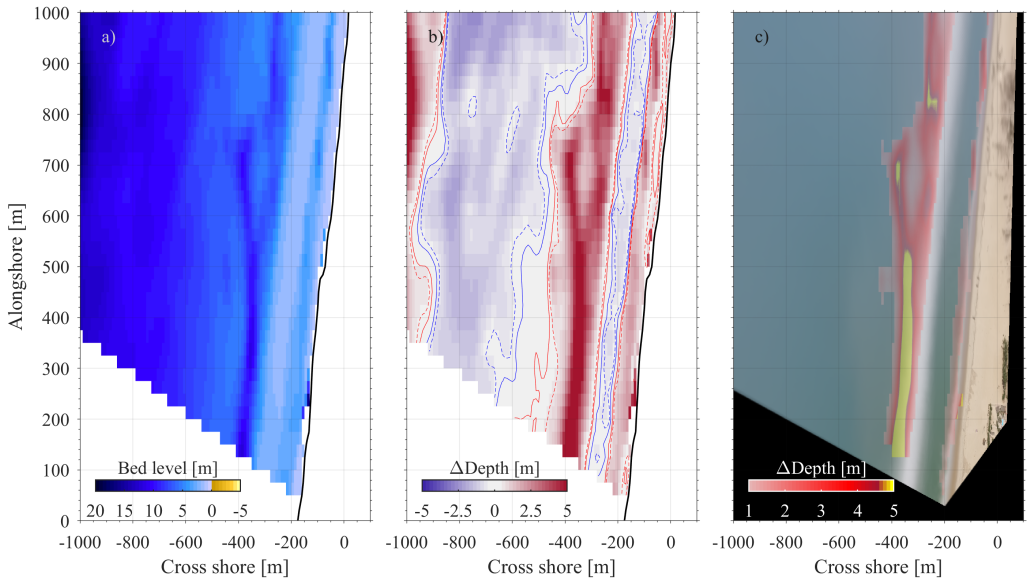

Figure 9: Depth estimation using the horizon and Google-Earth-picked GCPs

$$Im_{x,y,t} = \left| \frac{dI_{x,y,t}}{dt} \right| \tag{4}$$

in which Im represents the new intensity matrix, I is the former intensity matrix. Figure 10 shows the effect of (4) on a cross-shore timestack. In the timestack (Figure 10a), waves arrive from the left and propagate in time (down) to the right (shore). Wave breaking occurs between -600 and -400 m cross shore. Seawards (< -600 m) the wave signal is predominantly visible by the shadowed part (darker lines) while during/after the wave breaking process the wave signal has a much brighter pixel intensity. If (4) is applied to this timestack, the different wave signals are merged to a single representation of incident waves with brighter pseudo-pixel intensities, as shown in Figure 10b, and the phase shift is no longer present.

At this stage the implementation into cBathy remains in a testing phase. Hence, we feed the original signal and the modified signal simultaneously. Equation 4 is applied on the shallowest part of the domain from the wave breaking (> -600 m) inshore. Dominant frequencies are determined as in Holman et al. [10], but within the breaking zone the wave-phase fitting is performed on the modified signal. The result of the depth inversion using

the modified time-varying pixel intensities is presented in Figure 11

From Figure 11b,c it is apparent that around the breaking point error are significantly reduced. Over the whole camera footprint domain, RMS_{all} reduced from 2.35 to 1.28 m. Around breaking, at the edge of the surfzone, the RMS_{sz} was 3.1 m, after applying (4) this error is reduced to 1.3 m. Although the errors are more than halved, yet the largest errors are found at the wave-breaking region.

5. Conclusions

In this paper, we have applied bathymetry estimation to videos obtained from UAVs at St. Louis, Senegal. Before applying depth inversion techniques it is important to stabilise the full-video, to a single chosen frame (conveniently this could be the first frame). Traditionally, GCPs are measured in-situ with an RTK-GPS. Here we have shown that Google-Earth derived GCP-points in combination with horizon-derived roll can provide an

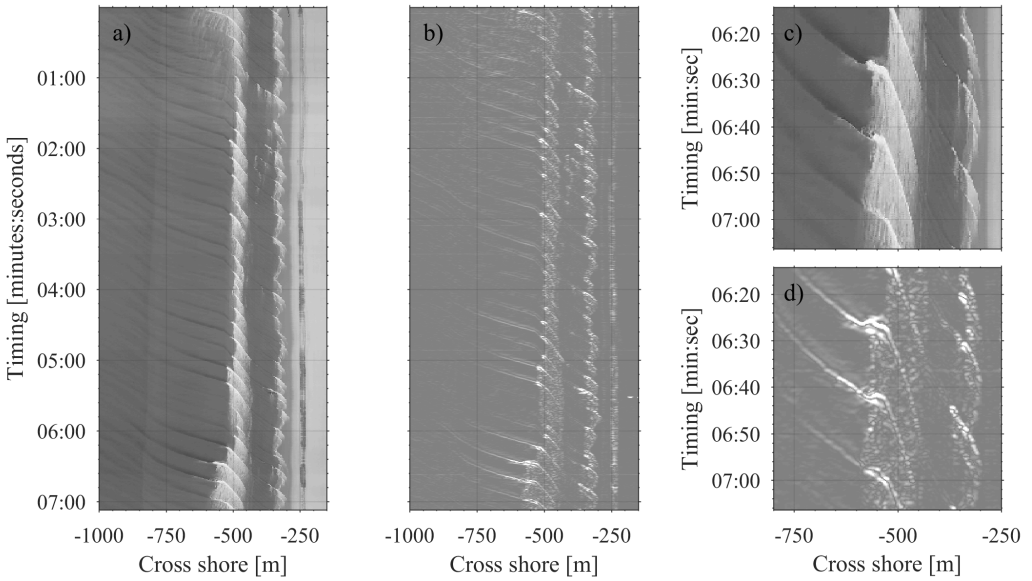

Figure 10: Effect of (4) spatio-temporal evolution of pixel intensity along an example cross-shore transect (timestack) at St. Louis. Offshore is on the left and the waves propagate inshore to the left and down in time. a) represents the timestack, b) is the result when (4) is applied to a). c) and d) show a close-up of respectively the timestack and the absolute derivative.

alternative way to estimate nearshore bathymetry, with a good level of accuracy. Our results show a strong over estimation seaward of wave breaking which is partially due to the Modulation Transfer Function. MTF issues can potentially be overcome by taking the absolute derivative in time for the pixel intensity. For our dataset, the image stabilisation and the break-point anomaly correction together reduce the overall error by over 45%. The break-point anomaly correction alone reduces the error around in the surfzone by 58%.

Acknowledgement

We are greatly indebted to the Aires Marines Protégées of Saint Louis for their logistic support during the field experiment and to Guillaume Detandt from Bordeaux University (EPOC) for providing the echo-sounder used for the bathymetric survey. Erwin Bergsma is currently funded by a post-doctoral fellowship of the French National Space Agency (Centre National d'Etudes Spatiales - CNES).

[1] E. D. Lazarus, M. A. Ellis, , A. B. Murray, D. M. Hall, An evolving

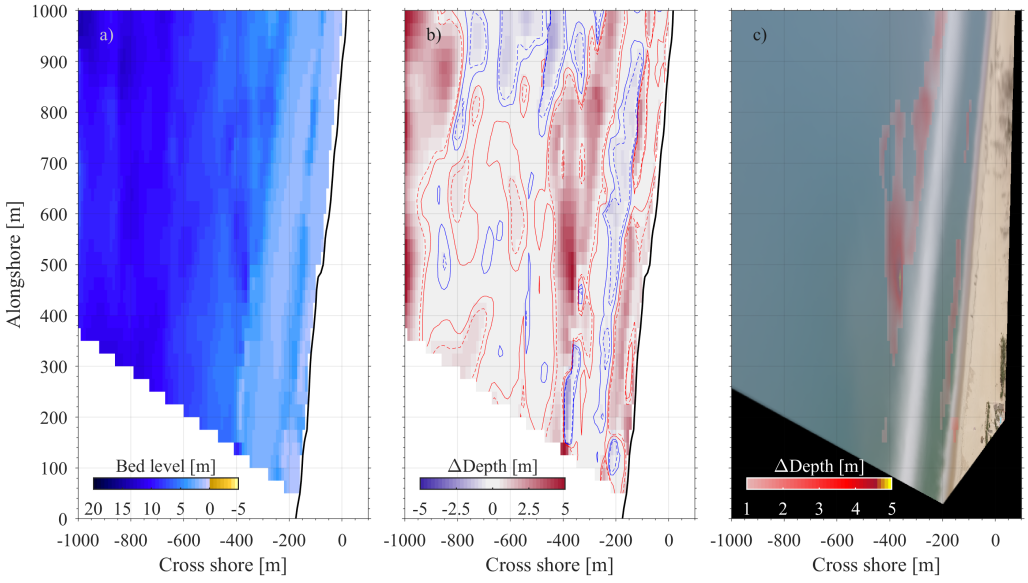

Figure 11: Estimated bathymetry using the breakpoint solution

research agenda for human-coastal systems, Geomorphology 256 (2016) pp. 81–90.

[2] M. D. Harley, I. L. Turner, A. D. Short, R. Ranasinghe, An empirical model of beach response to storms-se australia, in: Coasts and Ports 2009: In a Dynamic Environment.

[3] G. Coco, N. Sénechal, A. Rejas, K. Bryan, S. Capo, J. Parisot, J. Brown, J. MacMahan, Beach response to a sequence of extreme storms, Geomorphology 204 (2014) pp. 493–501.

[4] G. Masselink, B. Castelle, T. Scott, G. Dodet, S. Suanez, D. Jackson, F. Floc´h, Extreme wave activity during 2013/2014 winter and morphological impacts along the atlantic coast of europe, Geophysical Research Letters 43(5) (2016) pp. 2135–2143.

[5] K. L. Brodie, M. L. Palmsten, T. J. Hesser, P. J. Dickhudt, B. Raubenheimer, H. Ladner, S. Elgar, Evaluation of video-based linear depth inversion performance and applications using altimeters and hydrographic surveys in a wide range of environmental conditions, Coastal Engineering 136 (2018) pp. 147–160.

[6] R. A. Holman, K. L. Brodie, J. Nicholas J. Spore, Surf zone characterization using a small quadcopter: Technical issues and procedures, IEEE Transactions on Geoscience and Remote Sensing 55 (2017) pp. 2017–2027.

[7] E. W. J. Bergsma, R. Almar, Video-based depth inversion techniques, a method comparison with synthetic cases, Coastal Engineering 138 (2018) pp. 199–209.

[8] H. F. Stockdon, R. A. Holman, Estimation of wave phase speed and nearshore bathymetry from video imagery, Journal of geophysical Research 105 (2000) pp. 22015–22033.

[9] N. G. Plant, K. T. Holland, M. C. Haller, Ocean Wavenumber Estimation From Wave-Resolving Time Series Imagery, IEEE Transactions on Geosciences and Remote Sensing 46 (2008) pp. 2644–2658.

[10] R. A. Holman, N. Plant, T. Holland, cbathy: A robust algorithm for estimating nearshore bathymetry, J. Geophys. Res. Oceans 118 (2013) pp. 2595–2609.

[11] E. W. J. Bergsma, D. C. Conley, M. A. Davidson, T. J. O'Hare, Video-based nearshore bathymetry estimation in macro-tidal environments, Marine Geology 374 (2016) pp. 31–41.

[12] E. Anthony, Patterns of Sand Spit Development and Their Management Implications on Deltaic, Drift-aligned Coasts: the Cases of the Senegal and Volta River Delta Spits, West Africa, Spits, Sand and Gravel Spits, Coastal Research Library, Randazzo et al. (eds.), Springer, 2015.

[13] M. Sadio, E. J. Anthony, A. T. Diaw, P. Dussouillez, J. T. Fleury, A. Kane, R. Almar, E. Kestenare, Shoreline changes on the wave-influenced senegal river delta, west africa: The roles of natural processes and human interventions, Water 9 (2017).

[14] A. Ndour, R. A. Labi, M. Sadio, C. G. Degbe, A. T. Diaw, L. M. Oyd, E. J. Anthony, P. Dussouillez, H. Sambou, E. hadji Balla Diye, Management strategies for coastal erosion problems in west africa: Analysis, issues, and constraints drawn from the examples of senegal and benin, Ocean and Coastal Management 156 (2018) pp. 92–106.

[15] M. Schwendeman, J. Thomson, A horizon-tracking method for shipboard video stabilization and rectification, Journal of Atmospheric and Ocean Technology 32 (2015) pp. 164–176.

[16] R. Hartley, A. Zisserman, Multiple View Geometry in Computer Vision, Cambridge University Press, 2003.

[17] T. G. Farr, P. A. Rosen, E. Caro, R. Crippen, R. Duren, S. Hensley, M. Kobrick, M. Paller, E. Rodriguez, L. Roth, D. Seal, S. Shaffer, J. Shimada, J. Umland, M. Werner, M. Oskin, D. Burbank, D. Alsdorf, The shuttle radar topography mission, Rev. Geophys. 45 (2007).